Journal of Catalysis 311 (2014) 350–356

Contents lists available at ScienceDirect

Journal of Catalysis

journal homepage: www.elsevier.com/locate/jcat

Theoretical and kinetic assessment of the mechanism of ethane hydrogenolysis on metal surfaces saturated with chemisorbed hydrogen

David W. Flaherty [a,b,1], David D. Hibbitts [a,1], Elif I. Gürbüz [a], Enrique Iglesia [a,*]

[a] Department of Chemical Engineering, University of California at Berkeley, Berkeley, CA 94720, United States
[b] Department of Chemical and Biomolecular Engineering, University of Illinois at Urbana-Champaign, Urbana, IL 61801, United States

ARTICLE INFO

Article history:
Received 4 October 2013
Revised 20 November 2013
Accepted 29 November 2013

Keywords:
Alkanes
Hydrogenolysis
Reforming
Hydrogenation
Ring opening

ABSTRACT

Ethane hydrogenolysis involves C–C bond rupture in unsaturated species in quasi-equilibrium with gaseous reactants and H_2 on metal clusters, because C–C bonds weaken as C-atoms replace hydrogen with exposed metal atoms from catalyst surfaces. The nature and reactivity of such adsorbed species are probed here using kinetic data and density functional theory (DFT) for the case of Ir surfaces, but with conclusions that appear to be general to hydrogenolysis on noble metals. On surfaces saturated with chemisorbed H-atoms (H^*), theory and experiments indicate that C–C cleavage occurs predominantly via an α,β-bound $^*CHCH^*$ species that forms via sequential dehydrogenation of adsorbed ethane; all other intermediates cleave C–C bonds at much lower rates (>10^7-fold). Measured activation energies (213 kJ mol^{-1}) and free energies (130 kJ mol^{-1}) reflect the combined values for quasi-equilibrated steps that desorb H^*, adsorb C_2H_6, form C_2-intermediates by dehydrogenation, and form the transition state from $^*CHCH^*$ species. DFT-derived activation energies (218 kJ mol^{-1}) and free energies estimated from these values and statistical mechanics treatments of reaction and activation entropies (137 kJ mol^{-1}) are in excellent agreement with measured values. The removal of four H-atoms in forming the kinetically-relevant $^*CHCH^*$ intermediates, taken together with measured effects of H_2 pressure on hydrogenolysis rates, show that 2–3 H^* must be removed to bind this intermediate and the transition state, as expected from the structure of the proposed adsorbed species and H^* adsorption stoichiometries on Ir surface atoms that vary slightly with surface coordination on the non-uniform surfaces of metal clusters. Theory and experiments combine here to provide mechanistic insights inaccessible to direct observation and provide compelling evidence for reaction pathways long considered to be plausible for hydrogenolysis on noble metals. The extent of unsaturation in the single relevant intermediate and its C–C cleavage rates will depend on the identity of the metal, but the elementary steps and their kinetic relevance appear to be a general feature of metal-catalyzed hydrogenolysis.

1. Introduction

Hydrogenolysis of C–C bonds on metals is the reaction of choice for decreasing the chain length of acyclic molecules and for opening rings in cyclic hydrocarbons [1–12]. It is also responsible, however, for yield losses during hydrocarbon reforming and isomerization [13,14], making mechanistic models of hydrogenolysis reactivity and selectivity useful in practice [15]. C–C bond rupture has been widely used to probe the effects of cluster size [9,10,16–26], elemental identity, and alloying [27–37] in catalysis. Early studies recognized that hydrogenolysis requires the progressive weakening of C–C bonds through the formation of unsaturated intermediates that replace C–H bonds with C-metal bonds on surfaces [9,11,16,38–41]. The structure and degree of unsaturation of these species on metal surfaces have been inferred indirectly from measured effects of H_2 pressure on hydrogenolysis rates [29,38–40] and from isotopic exchange data [42–44], because they lack distinguishable spectroscopic signatures required for their direct interrogation and, therefore, can only be assessed using theoretical methods [35,45–48].

Our recent studies have addressed the enthalpic and entropic barriers that govern reactivity and selectivity in hydrogenolysis of C_2–C_{10} n-alkanes [49] and isoalkanes [50] on supported Ir clusters. Here, we combine hydrogenolysis turnover rates and their kinetic interpretation on Ir clusters saturated with chemisorbed hydrogen (H^*) with density functional theory (DFT) treatments on the Ir(1 1 1) surface in order to infer mechanistic details for the hydrogenolysis of ethane. This study shows that C–C bond cleavage occurs via a specific reactive intermediate ($^*CHCH^*$) that

* Corresponding author. Fax: +1 510 642 4778.
E-mail address: iglesia@berkeley.edu (E. Iglesia).
[1] These authors contributed equally to this work.

0021-9517/$ - see front matter © 2013 Elsevier Inc. All rights reserved.
http://dx.doi.org/10.1016/j.jcat.2013.11.026

forms by the loss of four H-atoms (as H_2) through the sequential dehydrogenation of adsorbed ethane molecules. These findings and the DFT-derived activation barriers agree well with measured turnover rates and activation energies on Ir clusters. They confirm the essential role of unsaturation in the cleavage of C–C bonds in ethane [45,46,48] and, by inference, in larger n-alkanes, isoalkanes, and cycloalkanes [7,8,16,35,47], for which similar kinetic dependences and activation barriers have been observed. The identification of the reactive species that cleave C–C bonds shows also how their concentrations depend on H_2 pressures and temperatures and can, therefore, inform the choice of reaction conditions and catalysts for processes that deliberately, or inadvertently, involve hydrogenolysis reactions.

2. Methods

2.1. Synthesis and characterization of Ir–SiO_2

Ir–SiO_2 (3.0 wt.%) was prepared by incipient wetness impregnation using reported methods [49]. Samples were heated to 393 K at 0.017 K s^{-1} in flowing dry air (Praxair, 99.99%, 5.0 cm^3 g^{-1} s^{-1}) and held for 8 h and subsequently heated at 0.033 K s^{-1} to 1123 K and held for 12 h. The sample was cooled to ambient temperature and then heated at 0.033 K s^{-1} to 1173 K in flowing 50% H_2/He (Praxair, 99.999%, 1.0 cm^3 g^{-1} s^{-1}) and held for 8 h. The sample was again cooled to ambient temperature and passivated in flowing 0.5% O_2/He (Praxair, 99.99%, 1.0 cm^3 g^{-1} s^{-1}) for 3 h. The number of exposed Ir atoms (Ir_s) was determined from volumetric uptakes of H_2, O_2, and CO at 298 K [49,51] and the mean Ir cluster diameter ($<d_{chem}>$) was estimated by assuming hemispherical crystallites and the atomic density of bulk Ir (70.7 atoms nm^{-3}) [52,53]. Ir fractional dispersions from H_2, O_2, and CO chemisorption were 0.13, 0.15, and 0.13, respectively, the average of which indicates that the mean diameter of the Ir clusters was 7 nm. Distribution of cluster sizes was determined by transmission electron microscopy (TEM) in bright-field mode (Philips, CM200F) using samples applied as a fine dust onto lacey carbon-coated Cu grids. Surface-averaged cluster diameters were calculated using the following:

$$< d_{TEM} >= \frac{\sum n_i d_i^3}{\sum n_i d_i^2} \quad (1)$$

where n_i is the number of clusters with a diameter d_i (1029 clusters) [54]. Values of $<d_{TEM}>$ (14.4 nm) and $<d_{chem}>$ (7 nm) indicate that the majority of the Ir exists in aggregates of $\sim 10^4$ atoms. We must conclude that, in this case, distributions of detected cluster sizes overestimate the mean cluster diameter because TEM does not detect a significant numbers of small ($d < 0.6$ nm) clusters that are represented in chemisorption experiments. Thus, we conclude that the chemisorption measurements most accurately represent the average size of the clusters, 7 nm, and the corresponding number of Ir_s is used to calculate hydrogenolysis turnover rates. The Ir content was measured by inductively-coupled plasma optical emission spectroscopy (Galbraith Laboratories, Inc.). The Supporting Information summarizes the synthesis and characterization of the 7 nm Ir–SiO_2 catalyst (Table S1) and contains a representative TEM image and cluster size distribution for the Ir–SiO_2 catalyst (Fig. S1).

2.2. Ethane hydrogenolysis rate measurements

Ethane hydrogenolysis rates were measured in a flow packed-bed stainless steel tubular reactor (3/8″ O.D.) with plug-flow hydrodynamics from 553 to 663 K with ethane ((C_2H_6)) and hydrogen ((H_2)) pressures from 10 to 80 kPa and from 0.6 to 1.8 MPa, respectively. The reactor was placed within a three-zone resistively-heated furnace, and the bed temperature was measured with a type K thermocouple held within a 1/16" stainless steel sheath aligned axially along the bed. The Ir–SiO_2 catalyst was mixed with additional SiO_2 (Cab–O–Sil HS-5, washed with deionized water and treated in flowing dry air at 793 K for 5 h) to avoid any axial or radial temperature gradients. Pressure was controlled using a dome-loaded regulator (Mity-Mite, S91XW). The catalyst was treated in flowing H_2 (Praxair, 99.999%) at ambient pressure (50 cm^3 g^{-1} s^{-1}) by heating to 673 K at 0.083 K s^{-1} and holding for 2 h. The composition of the reactant stream was set using electronic mass flow controllers (Parker, 201) to meter the flow rates of H_2 (Praxair, 99.999%), and ethane (5% ethane, 10% Ar, 85% He, Praxair, certified-grade). CH_4 and C_2H_6 effluent concentrations were measured by gas chromatography (Agilent GC, 5890) using a methyl silicone capillary column (HP-1, 50 m × 0.32 mm × 1.05 μm) and a flame ionization detector. No other hydrocarbons were detected. All rates are reported at differential conversions (<5%) to avoid consequential axial gradients in reactant concentrations. Turnover rates are reported as moles of ethane consumed per unit time normalized by the number of surface metal atoms determined by chemisorption, and reported uncertainties represent two-standard deviations (95% confidence intervals).

2.3. Computational methods

Periodic plane-wave DFT calculations were performed using the Vienna *ab initio* simulation package (VASP) [55–58]. The plane-waves were constructed using projector augmented-wave (PAW) potentials with an energy cutoff of 396 eV [59,60]. The revised Perdew–Burke–Ernzerhof (RPBE) form of the generalized gradient approximation (GGA) was used to determine exchange and correlation energies [61–63]. Calculations of gaseous species were computed using 18 × 18 × 18 Å unit cells. The catalyst surface was modeled as a 4 × 4 Ir(1 1 1) closed-packed periodic lattice with a lattice parameter of 3.84 Å; it consists of four layers in the *z*-direction with the bottom two layers fixed in their bulk positions and the other two allowed to relax to their minimum energy structures. Wavefunctions were converged to within 10^{-6} eV and forces were computed using a fast Fourier transform (FFT) grid with a cutoff of twice the planewave cutoff and a 3 × 3 × 1 Monkhorst–pack sampling of the first Brillouin zone (k-point mesh) [64]. For optimizations, the structures were relaxed until the force on unconstrained atoms was <0.05 eV/Å. After geometric convergence, a single-point calculation with a 6 × 6 × 1 k-point mesh was performed to optimize energy minima of reactant, product, and transition states.

Transition state (TS) structures were obtained for each elementary reaction by using the nudged elastic band (NEB) method [65,66] and the dimer method [67]. The NEB method was carried out using 16 images, and wavefunctions were converged to within 10^{-4} eV using a 3 × 3 × 1 k-point mesh and an FFT grid size of 1.5 times the planewave cutoff. The maximum force on each atom was converged to <0.3 eV/Å. These protocols provided an estimate of the reaction path and a starting point for the structure and the reactive vibrational mode for each transition state. The dimer algorithm was then used with wavefunctions converged to within 10^{-6} eV using a 3 × 3 × 1 k-point mesh and an FFT grid size of 2 times the planewave cutoff. For dimer calculations, the maximum force on each atom was converged to <0.05 eV/Å. As with optimizations of reactant and product states, the energy of the TS was then determined using a single-point calculation with 6 × 6 × 1 k-point mesh. Zero-point energy and thermal corrections were implemented using vibrational frequencies for reactants, transition states and products involved in each elementary step to estimate enthalpies and entropies of each state (details in Supporting information). For transition states, these frequency

analyses confirmed the transition state mode and the presence of a single negative frequency.

3. Results and discussion

Scheme 1 shows a sequence of elementary steps that account for measured rates for the hydrogenolysis of ethane [38–40,45,48,68], and which are analogous to steps for larger n-alkanes [17,49,69,70], and isoalkanes [17,27,50]. These steps are examined here by combining experimental rate data and DFT calculations. These elementary steps are consistent with the previously observed dependence of n-alkane hydrogenolysis rates on H_2 and n-alkane (C_2–C_{10}) pressures on clusters of Rh, Pt, as well as Ir, the latter being the focus of this study [49].

Scheme 1 includes H_2 dissociation (1.1), molecular C_2H_6 adsorption (1.2), and dehydrogenation of adsorbed C_2H_6 ($C_2H_6^*$, where * indicates an intermediate bound to one metal atom) via sequential C–H bond cleavage to form a quasi-equilibrated pool of dehydrogenated chemisorbed surface intermediates with y H-atoms removed from the ethane reactants ($^*C_2H_{6-y}^*$, where $1 \leqslant y \leqslant 6$ and *-* denotes an intermediate bound to two vicinal metal atoms; (1.3–1.5)). C–C bond rupture may occur in any of these $^*C_2H_{6-y}^*$ intermediates, which differ in both the number of H-atoms removed from ethane and the location from which they are removed. The presence of equilibrated mixtures of isobutane–isobutene [50] and cycloalkane–arene mixtures during hydrogenolysis on Ir [50,71] (and Pt, Ru, and Rh [72]) and the equilibrated nature of H/D exchange reactions during ethane hydrogenolysis on Pt [42], suggest that H_2 and ethane dissociation steps (steps 1.1–1.5) are indeed quasi-equilibrated, making C–C bond cleavage the sole kinetically-relevant step. Each surface intermediate ($^*C_2H_{6-y}^*$) cleaves C–C bonds with a rate constant that reflects, in part, the stability of the transition state that mediates that reaction event; thus, any of these unsaturated species ($^*C_2H_{6-y}^*$) can plausibly contribute to measured ethane hydrogenolysis rates. Some of these quasi-equilibrated intermediates will preferentially contribute to the products formed, because C–C bonds weaken as C–H bonds are replaced by C-metal bonds, in a process that transfers electron density from the C–C bond to the surface metal atoms [73]. Consequently, measured hydrogenolysis rates and their dependence on temperature and H_2 pressure ((H_2)) reflect the appropriately averaged degree of unsaturation of the intermediate pool and the stability of the respective transition states that lead to C–C bond cleavage in each of these intermediates.

Fig. 1 shows C_2H_6 hydrogenolysis turnover rates as a function of C_2H_6 (Fig. 1a) and H_2 (Fig. 1b) pressures on Ir clusters of 7 nm mean diameter. Hydrogenolysis rates are proportional to C_2H_6 pressure ($(C_2H_6)^{1.0\pm0.1}$, Fig. 1a) and show an inverse dependence on H_2 pressure ($(H_2)^{-3.3\pm0.2}$, Fig. 1b). Measured C_2H_6 hydrogenolysis rates (r_{obs}, Fig. 1) represent the combined rates of C–C bond cleavage for quasi-equilibrated reactive C_2-intermediates with each value of y:

$$r_{\text{obs}} = \sum_{y=0} r_y \tag{2}$$

where r_y is the rate of C–C cleavage of species with $(6 - y)$ H-atoms. The reactive species ($^*C_2H_{6-y}^*$) cleave C–C bonds at rates proportional to their respective surface concentrations:

$$r_y = k_{CC,y} \cdot [^*C_2H_{6-y}^*] \tag{3}$$

where $k_{CC,y}$ is the C–C cleavage rate constant. At high H_2:C_2H_6 ratios (>15), H* replaces dehydrogenated hydrocarbon species as the most abundant surface intermediate (MASI) as shown by hydrogenolysis rates that become inversely dependent on (H_2) for C_2–C_{10} n-alkanes

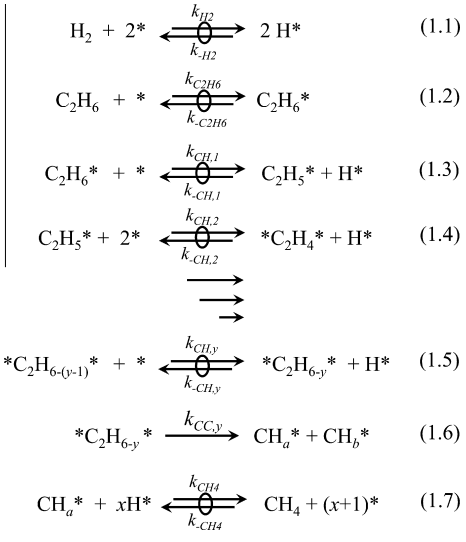

Scheme 1. Proposed sequence of steps and intermediates in ethane hydrogenolysis on Ir clusters. (* denotes an unoccupied surface site; *-* an intermediate bound to two vicinal metal atoms; k_x and k_{-x} are kinetic constants for each forward and reverse step).

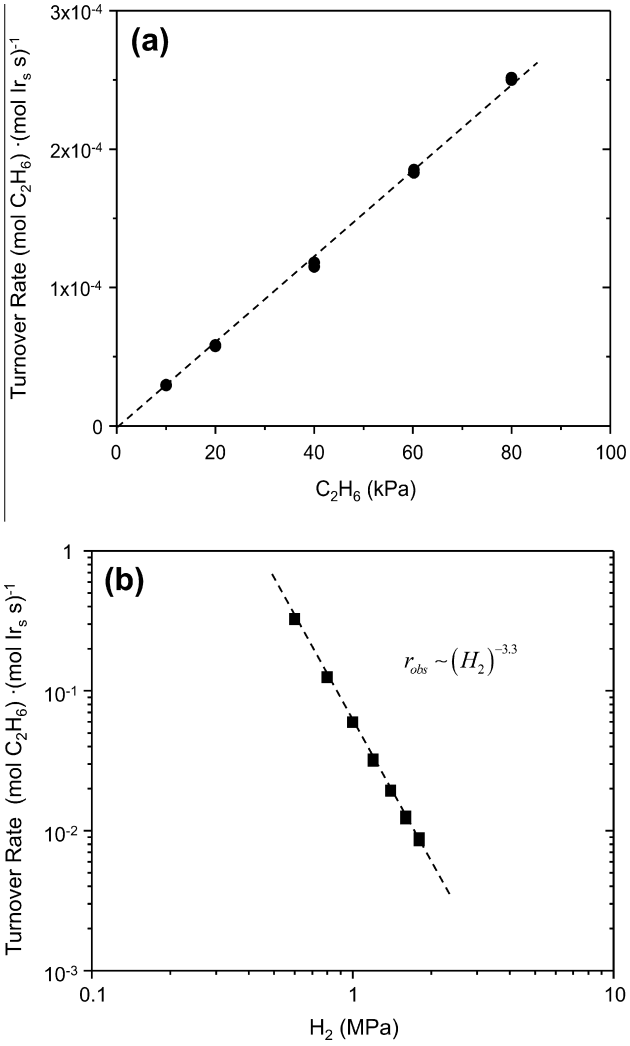

Fig. 1. Hydrogenolysis turnover rates on 7 nm Ir–SiO_2 clusters at 593 K. Effects of: (a) C_2H_6 pressure at 1.8 MPa H_2, and (b) H_2 pressure at 20 kPa C_2H_6.

[49]. In this case, the rate equation derived from elementary steps in Scheme 1, taken together with the assumption of quasi-equilibrated molecular adsorption and dehydrogenation steps (steps 1.1–1.5) [49], becomes:

$$r_y = k_{CC,y} \cdot \frac{\left(\prod_{n=1}^{y} K_{CH,n}\right) \cdot K_{C_2H_6} \cdot (C_2H_6)}{K_{H_2} \cdot (H_2)^{\lambda}} \cdot [L] \quad (4)$$

Here, K_{H_2} and $K_{C_2H_6}$ are the equilibrium constants for adsorption of H_2 and C_2H_6, respectively and $\prod_{n=1}^{y} K_{CH,n}$ represents the product of the equilibrium constants for the sequential C–H bond ruptures that occur as C_2H_6 dehydrogenates before C–C bond cleavage in each intermediate. This equation is consistent with measured hydrogenolysis turnover rates, which are proportional to (C_2H_6) (Fig. 1a) and decrease with increasing H_2 pressure (Fig. 1b). The value of λ (3.3 ± 0.2, from the data in Fig. 1b) in Equation (4) reflects the combination of the number of H*-atoms that desorb from the surface (γ) to accommodate the reactive intermediate (reverse of step 1.1) and the number of H-atoms lost from C_2H_6 to form reactive species that cleave C–C bonds (y, steps 1.3–1.5) [49] according to the equation:

$$y + \gamma = 2\lambda \quad (5)$$

where λ must be multiplied by a factor of two because λ represents the number of H_2 molecules while y and γ are the number of H-atoms. The chemical interpretation of λ values is identical on H*-covered surfaces of other metal clusters (e.g., 0.7 nm Ir, 3.0 ± 0.2 [49]; 0.9 nm Rh, 3.0 ± 0.2 [49]; 0.6 nm Pt, 2.3 ± 0.2 [49]; and 1.0 nm Ru, 3.0 ± 0.2 [72]). These values show that C–C bonds are cleaved in deeply dehydrogenated intermediates derived from C_2H_6 on metal cluster catalysts. This conclusion is consistent with previous findings that have shown that multiple H-atoms are lost from C_2H_6 before the C–C bond cleaves on metal surfaces [28,38,74]. The chemical significance of the dependence of rates on (H_2) is less clear for $C_2H_x^*$-covered surfaces (hydrocarbons as MASI) or surfaces containing both free sites and $C_2H_x^*$-species [28,38], because the average H-content of the surface intermediates and the H-content of the reactive intermediates are both unknown [49].

Ethane hydrogenolysis rates show that an average of 6.6 ± 0.4 H-atoms evolve as H_2 during the formation of the reactive intermediates that undergoes C–C bond cleavage on 7 nm Ir clusters (Fig. 1b). The non-integer nature of the reactivity-averaged value of y would indicate that several intermediates, with different H-contents (Eq. (2), e.g., *CHCH* and *CHC*), have transition states with similar stability, thus cleaving C–C bonds at comparable rates. Non-integer γ values would show that multiple pairs of exposed Ir atoms, distinct in their H*-coverage, contribute to measured rates. For example, ensembles that include edge and corner atoms, can bind more than one H-atom ($H/Ir_s > 1$) [75–77], and would give a different γ than ensembles containing only terrace sites, which bind a single H-atom. Alternatively, the rates could be dominated by C–C bond rupture that occurs entirely on ensembles of terraces sites, in which case, fractional γ values show that a significant number of terrace sites are unoccupied (i.e., $H/Ir_s < 1$) at the equilibrium H*-coverages for these experiments (0.6–1.8 MPa, 593 K). Measurements of hydrogenolysis rates, by themselves, cannot determine y and γ values; therefore, they cannot discern whether parallel pathways or distinct site occupancy account for turnovers that release a non-integer average number of H-atoms into the gas-phase. We examine these possibilities by using quantum mechanical simulations to assess the stability of transition states that cleave C–C bonds in C_2-intermediates derived from C_2H_6 adsorption and subsequent dehydrogenation on bare Ir(1 1 1) with the implicit assumption that the presence of H*-atoms at saturation coverages do not cause significant differences between the stability of different surface intermediates and transition states and do not change differences between the barriers to activate C–C bonds in different intermediates. The Ir(1 1 1) surface was selected because it is representative of the majority of the surface of 7 nm Ir clusters at low temperatures and in vacuum. These calculations will not account for reactivity of the minor fraction (<10% [78]) of under-coordinated sites that exist on the surfaces of these clusters. Turnover rates for C_2H_6 hydrogenolysis on these under-coordinated sites, which dominate the surfaces of 0.7 nm Ir clusters, are, however, ~200 times smaller [49] than turnover rates on 7 nm Ir clusters at 20 kPa C_2H_6, 1.8 MPa H_2, 593 K. Thus, we estimate that Ir atoms that are located at edges and corners of 7 nm Ir clusters account for ~0.05% of the measured C_2H_6 hydrogenolysis rate, and consequently, that the Ir(1 1 1) surface provides a reasonable and appropriate description of the cluster surfaces that contribute to measured hydrogenolysis rates.

C–C bond cleavage in partially-dehydrogenated C_2-intermediates (Scheme 1) is preceded by quasi-equilibrated adsorption of C_2H_6 and H_2 and dehydrogenation of C_2H_6. On H*-saturated surfaces, these elementary steps lead to overall enthalpy barriers ($\Delta H^{\ddagger}$) given by the enthalpy of the transition state ($H^{\ddagger}$) and the λ moles of H_2 formed by dehydrogenating ethane on the surface ($\lambda \cdot H_{H2}$) relative to the combined enthalpies of the relevant precursors (H_{ref}). In this case, the relevant precursors are the gaseous ethane reactant (H_{C2H6}) and the γ H*-atoms displaced from the Ir surface to accommodate the transition state ($\gamma \cdot H_{H*}$), as shown by the functional form of the rate expression Eq. (4). Thus, the state properties of enthalpy show that $\Delta H^{\ddagger}$ is given by:

$$\Delta H^{\ddagger} = H^{\ddagger} + \lambda \cdot H_{H2} - H_{ref} = H^{\ddagger} + \lambda \cdot H_{H2} - H_{C2H6} - \gamma \cdot H_{H^*} \quad (6)$$

The value of $\Delta H^{\ddagger}$ must also be equal to the sum of reaction enthalpies (H_{rxn}) for all steps preceding the kinetically-relevant transition state and the intrinsic activation enthalpy (H_{act}) to form the TS from the reactive intermediate:

$$\Delta H^{\ddagger} = \sum H_{rxn} + H_{act} \quad (7)$$

Overall entropy changes ($\Delta S^{\ddagger}$) are also state functions and are similarly defined:

$$\Delta S^{\ddagger} = S^{\ddagger} + \lambda \cdot S_{H2} - S_{ref} = S^{\ddagger} + \lambda \cdot S_{H2} - S_{C2H6} - \gamma \cdot S_{H*} \quad (8)$$

$$\Delta S^{\ddagger} = \sum S_{rxn} + S_{act} \quad (9)$$

These equations lead, in turn, to overall free energy barriers ($\Delta G^{\ddagger}$):

$$\Delta G^{\ddagger} = \Delta H^{\ddagger} - T\Delta S^{\ddagger} \quad (10)$$

for ethane hydrogenolysis reactions.

Fig. 2 shows H_{rxn} and H_{act} for C–H and C–C bond rupture in C_2H_6 and its dehydrogenated intermediates (steps 1.3–1.6) calculated by DFT on bare Ir(1 1 1) surfaces at 593 K. When H* is the MASI, the formation and activation of $^*C_2H_{6-y}^*$ species on two adjacent sites (*-*) is preceded by the recombinative desorption of vicinal H* (step 1.1, H_{rxn} = 34 kJ mol^{-1}). In these simulations, C–C cleavage can occur via interactions of C_2H_6 with *-* site pairs to form two CH_3^* fragments (H_{act} = 200 kJ mol^{-1}) but, oxidative metal–atom insertion into the C–H bond to form adsorbed ethyl ($CH_3CH_2^*$) and H* involves a much smaller barrier (H_{act} = 99 kJ mol^{-1}). After this initial C–H activation step, $CH_3CH_2^*$ can react with an unoccupied site to cleave the C–C bond and form CH_3^* and CH_2^* (H_{act} = 136 kJ mol^{-1}), but its dehydrogenation to form CH_3CH^* (H_{act} = 29 kJ mol^{-1}) or $^*CH_2CH_2^*$ (H_{act} = 46 kJ mol^{-1}) or its hydrogenation by H* to re-form $CH_3CH_3^*$ (H_{act} = 18 kJ mol^{-1}) are more facile. Differences between the barrier to cleave the C–C bond and to form or cleave C–H bonds (>90 kJ mol^{-1}) indicate that $CH_3CH_2^*$ formation is quasi-equilibrated during ethane hydrogenolysis.

H_{rxn} and H_{act} for C–C and C–H bond cleavage were calculated for all surface intermediates from $C_2H_5^*$ to $^*C_2^*$ (Fig. 2, and SI, Figs.

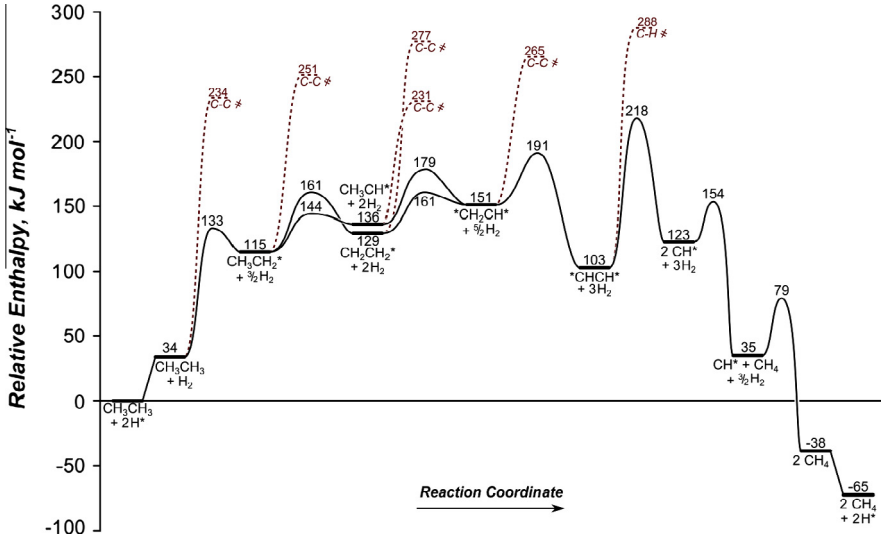

Fig. 2. DFT-derived reaction enthalpy diagram for ethane hydrogenolysis on an Ir(1 1 1) surface at 593 K. Dashed lines show barriers for unfavorable C–C and C–H bond activation transition states. The intermediates CH_3C^* and $^*CH_2C^*$ are omitted for clarity, but are shown in SI (Figs. S8 and S10).

Table 1
DFT-derived effective energy ($\Delta E^{\ddagger}$), zero-point energy corrected effective energy ($\Delta E_Z^{\ddagger}$), enthalpy ($\Delta H^{\ddagger}$), entropy ($\Delta S^{\ddagger}$), and free energy ($\Delta G^{\ddagger}$) of each kinetically-relevant C–C bond activation of the equilibrated pool of dehydrogenated intermediates. Reaction enthalpy diagrams, similar to Fig. 2, are shown for C–C activation via each intermediate in Figs. S3–S12.

Reaction	$\Delta E^{\ddagger}$ [a] kJ mol^{-1}	$\Delta E_Z^{\ddagger}$ [a] kJ mol^{-1}	$\Delta H^{\ddagger}$ [b] kJ mol^{-1}	$\Delta S^{\ddagger}$ [b] J mol^{-1} K^{-1}	$\Delta G^{\ddagger}$ [b] kJ mol^{-1}	λ H_2	$\frac{r}{[L]}$ [c] C_2H_6 Ir_s^{-1} s^{-1}
$CH_3CH_3 + 2^* \rightarrow 2CH_3^*$	257	225	234	-123	307	1.0	1.2×10^{-16}
$CH_3CH_2^* + * \rightarrow CH_3^* + CH_2^*$	273	240	251	-66	291	1.5	7.6×10^{-16}
$CH_3CH^* + {}^* \rightarrow CH_3^* + CH^*$	260	211	231	5	229	2.0	5.2×10^{-11}
$^*CH_2CH_2^* \rightarrow 2CH_2^*$	306	257	277	6	274	2.0	5.6×10^{-15}
$^*CH_2CH^* \rightarrow CH_2^* + CH^*$	293	226	265	50	236	2.5	3.0×10^{-12}
$^*CH_3C^* \rightarrow CH_3^* + C^*$	320	255	281	74	237	2.5	2.4×10^{-12}
$^*CH_2C^* \rightarrow CH_2^* + C^*$	408	327	358	133	279	3.0	1.2×10^{-16}
$^*CHCH^* \rightarrow 2CH^*$	269	190	218	136	137	3.0	3.7×10^{-4}
$^*CHC^* \rightarrow CH^* + C^*$	401	307	340	184	231	3.5	4.6×10^{-13}
$^*CC^* \rightarrow 2C^*$	536	425	465	257	313	4.0	6.6×10^{-21}
Experiment	–	–	213 ± 2	141 ± 5	130 ± 5	3.3 ± 0.2	6.5×10^{-4}

[a] Calculated at 0 K, vacuum.
[b] Determined at 593 K, 101.3 kPa (see Supporting information).
[c] From Equation (12) using 593 K, 20 kPa C_2H_6, 1.8 MPa H_2.

S2–S11). Table 1 lists the $\Delta H^{\ddagger}$ and $\Delta G^{\ddagger}$ values, calculated from Eq. (7) and Eq. (10), respectively, for C–C bond cleavage in each of the 10 C_2-intermediates. The formation and cleavage of C–H bonds is favored by >50 kJ mol^{-1} over C–C bond cleavage for all $^*C_2H_{6-y}^*$ species, except *CHCH* intermediate. C–C bond cleavage in this *CHCH* intermediate shows a much lower activation barrier (H_{act} = 105 kJ mol^{-1}) than for its further dehydrogenation (H_{act} = 185 kJ mol^{-1}), indicating that *CHCH* is the dehydrogenated intermediate predominantly responsible for measured ethane hydrogenolysis turnover rates. H_{act} values for its hydrogenation steps to re-form $C_2H_6^*$ are lower than its H_{act} for C–C bond cleavage by >25 kJ mol^{-1}, consistent with quasi-equilibrated *CHCH* formation from C_2H_6. These conclusions are consistent with measured hydrogenolysis rates (Fig. 1) and with the rate equation Eq. (4), and its chemical interpretation [49].

The formalism of transition state theory [79] dictates that the gas-phase C_2H_6 and two H*-atoms exist in quasi-equilibrium with the transition state that cleaves the C–C bond ($^*C_2H_{6-y}^*\ddagger$) and the product H_2:

$$C_2H_6 + \gamma \cdot H^* \overset{K^{\ddagger}}{\rightleftarrows} {*}C_2H_{6-y}{*}\ddagger + \lambda \cdot H_2 \qquad (11)$$

where $K^{\ddagger}$ is the equilibrium constant describing the overall equilibrium between these reactants and products. Hydrogenolysis rates for each reactive intermediate (Table 1) are calculated at 20 kPa C_2H_6, 1.8 MPa H_2, and 593 K using the functional form of the rate expression derived from transition state theory:

$$\frac{r}{[L]} = \frac{k_B T}{h} \cdot exp^{\left(\frac{-\Delta G_i^{\ddagger}}{RT}\right)} \cdot \frac{(C_2H_6)}{(H_2)^{\lambda}} \qquad (12)$$

Here, k_B and h are the Boltzmann and Planck constant, respectively, and $\Delta G_i^{\ddagger}$ and λ have values that depend on the intermediate (Table 1). Turnover rates reflect the reactivity of multiple intermediates only when their C–C bonds rupture at comparable rates Eq. (12). DFT-derived barriers (Table 1) show that the enthalpy barrier for cleaving C–C bonds in *CHCH* ($\Delta H^{\ddagger}$ = 218 kJ mol^{-1}) is 13 kJ mol^{-1} smaller than for the next most reactive intermediate (CH_3CH^*, $\Delta H^{\ddagger}$ = 231 kJ mol^{-1}). Differences in $\Delta G^{\ddagger}$ values for different reactive intermediates, which determine rate constants, also reflect the significant entropy gained from gas-phase H_2 formed by quasi-equilibrated dehydrogenation of C_2H_6 and desorption of H* from the surface [49]. As a result of entropy differences, it is far more favorable to cleave the C–C bond in *CHCH* ($\Delta G^{\ddagger}$ = 137 kJ mol^{-1}) rather

than in CH_3CH^* ($\Delta G^\ddagger$ = 229 kJ mol^{-1}) or any other intermediate (Table 1), because more deeply dehydrogenated intermediates produce a larger number of gaseous H_2 molecules, giving larger entropy gains (Table 1), which decrease $\Delta G^\ddagger$ (Eq. (10)). Calculated barriers for C–C bond cleavage in $^*CHCH^*$ ($\Delta H^\ddagger$ = 218 kJ mol^{-1}, $\Delta G^\ddagger$ = 137 kJ mol^{-1}) agree within 10 kJ mol^{-1} with measured barriers for C_2H_6 hydrogenolysis ($\Delta H^\ddagger$ = 213 ± 2 kJ mol^{-1}, $\Delta G^\ddagger$ = 130 ± 5 kJ mol^{-1}, Table 1); these experimental barriers were determined from changes in hydrogenolysis turnover rates with temperature (Fig. 3) on surfaces of 7 nm Ir clusters, which predominantly consist of close-packed (1 1 1) terraces [78]. The predicted rates for C–C bond cleavage in all possible reactive intermediates (Table 1) show that differences in $\Delta G^\ddagger$ lead to much higher C–C bond cleavage rates in $^*CHCH^*$ (3.7×10^{-4} C_2H_6 Ir_s^{-1} s^{-1}) than for any other species in the quasi-equilibrated pool of unsaturated intermediates (e.g., CH_3CH^*, 5.2×10^{-11} C_2H_6 Ir_s^{-1} s^{-1}) (20 kPa C_2H_6, 1.8 MPa H_2, 593 K). These computational and experimental results, summarized in Fig. 4, show that measured hydrogenolysis turnover rates predominantly reflect C–C bond rupture in a single intermediate, $^*CHCH^*$, at the experimental conditions. Thus, the value of y in Eq. (5) is equal to four.

DFT calculations show that measured hydrogenolysis rates reflect C–C cleavage rates in $^*CHCH^*$, therefore, four of the 6.6 ± 0.4 H-atoms that desorb come from dehydrogenating C_2H_6. This requires that the other 2.6 ± 0.4 H-atoms desorb from the catalyst surface (i.e., γ = 2.6 ± 0.4; Eq. (5)). This fractional value of γ indicates that H*-coverages are not uniform at all sites on 7 nm Ir clusters. A plausible interpretations involves ensembles of surface atoms that require either two or three H* to desorb depending on the coordination of exposed atoms on non-uniform Ir clusters. Edge and corner atoms of Ir nanoparticles have larger H/Ir_s adsorption stoichiometries than terraces at all H*-coverages, as shown by our DFT calculations on Ir_{201} cubo-octahedral nanoparticles (1.6 nm in diameter, Fig. S2), DFT calculations on <1 nm Pt clusters [76], and experiments with Ir, Rh, and Pt clusters (<1.5 nm in diameter) [77]. The agreement between measured and DFT-derived $\Delta G^\ddagger$ values (Table 1) and turnover rates (Fig. 4) indicates that hydrogenolysis occurs predominantly via the $^*CHCH^*$ reactive intermediate and that fractional γ values are likely to reflect differences between the H/Ir_s among distinct active site ensembles on Ir cluster surfaces.

C_2H_6 hydrogenolysis rates on H*-covered Ir clusters and their kinetic dependence on reactant pressure and temperature and

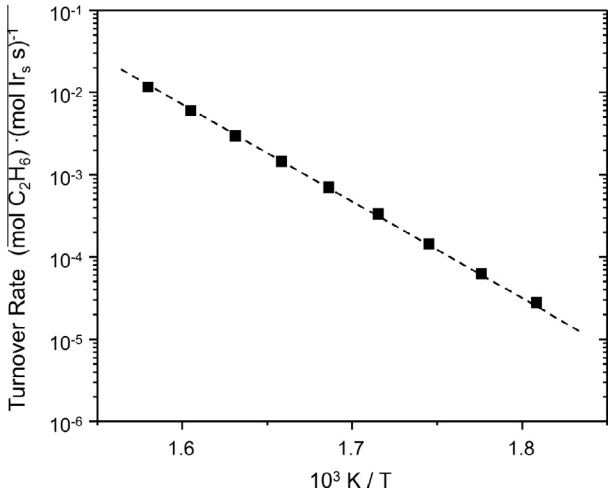

Fig. 3. Change in ethane hydrogenolysis turnover rate with reciprocal temperature on hydrogen-covered surfaces of 7 nm Ir–SiO_2 clusters at 20 kPa C_2H_6, 1.8 MPa H_2, 553–633 K.

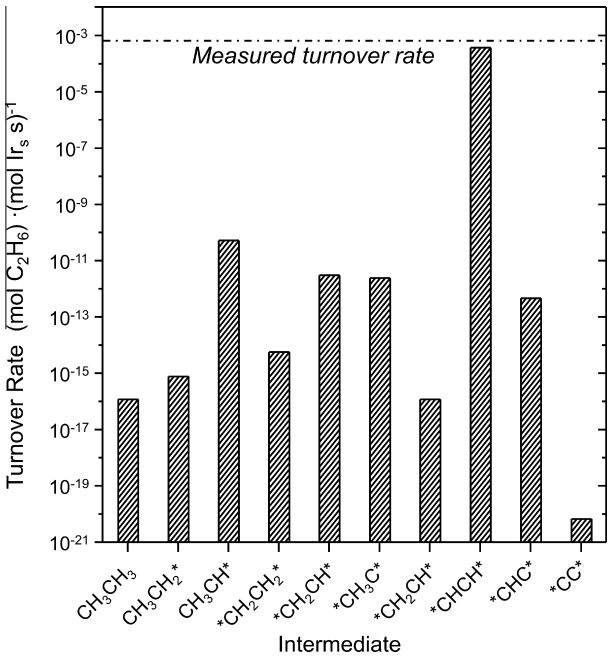

Fig. 4. Turnover rates (logarithmic scale) for C–C bond rupture in all C_2-intermediates, calculated from Eq. (12), using $\Delta G^\ddagger$ from DFT calculations for the Ir(1 1 1) surface, and experimentally measured turnover rate at these conditions on 7 nm Ir clusters (dashed line) at 20 kPa C_2H_6, 1.8 MPa H_2, 593 K.

DFT-derived energy and free energy barriers for C–H and C–C bond cleavage on Ir(1 1 1) indicate that C–C cleavage occurs predominantly in a single reactive intermediate because of C–H and C–C bond activation barriers that vary with the H-content of C_2-species. Chemical similarities between alkanes suggest that hydrogenolysis rates for a given C–C bond in larger n-alkanes [49], isoalkanes [50], and cycloalkanes [50,71] will also arise from the rupture of a C–C bond within a small fraction of all unsaturated surface intermediates. The quasi-equilibrated nature of the intervening adsorption and dehydrogenation steps provide opportunities to control the position of C–C bond cleavage in larger alkane reactants by controlling H_2 pressures, which concomitantly change the relative coverages of intermediates with different degrees of unsaturation. Differences between C–H and C–C activation barriers will change with the elemental identity of metal clusters and cause the H-content of reactive intermediates to differ among catalysts [27–37]. In spite of this, even very small differences in $\Delta G^\ddagger$ at typical temperatures for hydrogenolysis will cause C–C bond cleavage to occur predominately in a single unsaturated species [9,11,16,38–41].

4. Conclusions

Overall activation parameters ($\Delta H^\ddagger$, $\Delta S^\ddagger$, $\Delta G^\ddagger$) to cleave the C–C bond in ethane-derived C_2 surface intermediates were calculated by DFT and compared to measurements that reflect the composition of the reactive species and the $\Delta G^\ddagger$ for the dominant reaction pathway. This comparison was possible because hydrogenolysis turnover rates were measured in the limit of well-defined coverages (H* as MASI) on 7 nm Ir particles for which the predominant surfaces are similar to the (1 1 1) plane modeled in simulations. Results from DFT confirm that C_2H_6 undergoes quasi-equilibrated dehydrogenation steps, forming a pool of dehydrogenated intermediates prior to C–C bond cleavage. Each C_2-intermediate can undergo irreversible and kinetically-relevant C–C activation to form C_1 intermediates which are then rapidly hydrogenated to form CH_4. The rates at which each intermediate cleaves its C–C bond de-

pends upon the free energy of its distinct transition state, therefore, experimental rates can potentially reflect the sum of C–C bond cleavage rates within multiple and distinct reactive species. Large differences between $\Delta G^{\ddagger}$ for C–C bond rupture in different reactive intermediates indicate, however, that C_2H_6 hydrogenolysis is dominated by the contributions of a single intermediate ($^*CHCH^*$) on Ir clusters. The number of H^*-atoms that are displaced when the C–C bond in $^*CHCH^*$ cleaves varies between two to three, as it depends on the local H^*-coverage which varies across the surface of Ir clusters. This study focuses on the relatively simple system of C_2H_6 hydrogenolysis on large clusters of Ir, yet it establishes a methodology to effectively combine experiment and theory in order to study hydrogenolysis of complex alkanes and other reactants on metal clusters of different elements and sizes.

Acknowledgments

The authors acknowledge Dr. Chris Kliewer (ExxonMobil) for the TEM images, Dr. Stuart L. Soled (ExxonMobil) for helpful guidance in catalyst synthesis and characterization, Ms. Sarika Goel for careful review of this manuscript, and Mr. Omar Kunbargi (UC-Berkeley) for assistance in acquiring rate data. We are grateful to ExxonMobil Research and Engineering Company for partial financial support of the research described in this manuscript. We also dedicate this manuscript to the memory of Dr. John H. Sinfelt, who for many decades acted as an intellectual beacon for conceptual advances in catalysis.

Appendix A. Supplementary material

Supplementary data associated with this article can be found, in the online version, at http://dx.doi.org/10.1016/j.jcat.2013.11.026.

References

[1] J. Weitkamp, P.A. Jacobs, J.A. Martens, Appl. Catal. 8 (1983) 123–141.
[2] G.B. McVicker, M. Daage, M.S. Touvelle, C.W. Hudson, D.P. Klein, W.C. Baird, B.R. Cook, J.G. Chen, S. Hantzer, D.E.W. Vaughan, E.S. Ellis, O.C. Feeley, J. Catal. 210 (2002) 137–148.
[3] P.T. Do, W.E. Alvarez, D.E. Resasco, J. Catal. 238 (2006) 477–488.
[4] S. Dokjampa, T. Rirksomboon, D.T.M. Phuong, D.E. Resasco, J. Mol. Catal. A: Chem. 274 (2007) 231–240.
[5] R.J. Fenoglio, G.M. Nunez, D.E. Resasco, Appl. Catal. 63 (1990) 319–332.
[6] M. Santikunaporn, W.E. Alvarez, D.E. Resasco, Appl. Catal., A 325 (2007) 175–187.
[7] H. Shi, O.Y. Gutierrez, G.L. Haller, D. Mei, R. Rousseau, J.A. Lercher, J. Catal. 297 (2013) 70–78.
[8] H. Shi, X. Li, G.L. Haller, O.Y. Gutierrez, J.A. Lercher, J. Catal. 295 (2012) 133–145.
[9] F.G. Gault, C. R. Hebd. Seances. Acad. Sci. 245 (1957) 1620–1623.
[10] G. Maire, C. Corolleu, D. Juttard, F.G. Gault, J. Catal. 21 (1971) 250–253.
[11] G. Maire, G. Plouidy, J.C. Prudhomme, F.G. Gault, J. Catal. 4 (1965) 556–569.
[12] F. Weisang, F.G. Gault, J. Chem. Soc.-Chem. Commun. (1979) 519–520.
[13] J.G. Speight, Petroleum refinery processes, in: R.E. Kirk, D.F. Othmer (Eds.), Kirk-Othmer Encyclopedia of Chemical Technology, John Wiley and Sons Inc, New York, 2012, pp. 1–49.
[14] E. Iglesia, S.C. Reyes, R.J. Madon, S.L. Soled, Adv. Catal. 39 (1993) 221–302.
[15] G.C. Bond, Metal-Catalysed Reactions of Hydrocarbons, Springer, New York, 2005.
[16] F.G. Gault, Adv. Catal. 30 (1981) 1–95.
[17] J.R. Engstrom, D.W. Goodman, W.H. Weinberg, J. Am. Chem. Soc. 110 (1988) 8305–8319.
[18] D.W. Goodman, Surf. Sci. 123 (1982) L679–L685.
[19] S.L. Anderson, J. Szanyi, M.T. Paffett, A.K. Datye, J. Catal. 159 (1996) 23–30.
[20] D. Kalakkad, S.L. Anderson, A.D. Logan, J. Pena, E.J. Braunschweig, C.H.F. Peden, A.K. Datye, J. Phys. Chem. 97 (1993) 1437–1444.
[21] F. Zaera, G.A. Somorjai, J. Phys. Chem. 89 (1985) 3211–3216.
[22] G.C. Bond, J.C. Slaa, J. Mol. Catal. 89 (1994) 221–228.
[23] G.C. Bond, R. Yahya, B. Coq, J. Chem. Soc.-Faraday Trans. 86 (1990) 2297–2301.
[24] P.S. Kirlin, B.C. Gates, Nature 325 (1987) 38–40.
[25] G.C. Bond, A.D. Hooper, Appl. Catal., A 191 (2000) 69–81.
[26] G.A. Del Angel, B. Coq, R. Dutartre, F. Figueras, J. Catal. 87 (1984) 27–35.
[27] M. Boudart, L.D. Ptak, J. Catal. 16 (1970) 90–96.
[28] J.H. Sinfelt, J. Catal. 27 (1972) 468–471.
[29] J.H. Sinfelt, W.F. Taylor, D.J.C. Yates, J. Phys. Chem. 69 (1965) 95–101.
[30] J.H. Sinfelt, D.J.C. Yates, J. Catal. 10 (1968) 362–367.
[31] J.H. Sinfelt, D.J.C. Yates, J.L. Carter, J. Catal. 24 (1972) 283–296.
[32] D.J.C. Yates, J.H. Sinfelt, J. Catal. 14 (1969) 182–186.
[33] J.H. Sinfelt, Acc. Chem. Res. 10 (1977) 15–20.
[34] P. Samoila, M. Boutzeloit, C. Especel, F. Epron, P. Marecot, Appl. Catal., A 369 (2009) 104–112.
[35] M. Chia, Y.J. Pagan-Torres, D. Hibbitts, Q. Tan, H.N. Pham, A.K. Datye, M. Neurock, R.J. Davis, J.A. Dumesic, J. Am. Chem. Soc. 133 (2011) 12675–12689.
[36] B. Coq, E. Crabb, F. Figuéras, J. Mol. Catal. A: Chem. 96 (1995) 35–48.
[37] H.C. De Jongste, V. Ponec, F.G. Gault, J. Catal. 63 (1980) 395–403.
[38] A. Cimino, M. Boudart, H. Taylor, J. Phys. Chem. 58 (1954) 796–800.
[39] C. Kemball, H.S. Taylor, J. Am. Chem. Soc. 70 (1948) 345–357.
[40] K. Morikawa, W.S. Benedict, H.S. Taylor, J. Am. Chem. Soc. 58 (1936) 1795–1800.
[41] J.H. Sinfelt, Adv. Catal. 23 (1973) 91–119.
[42] R.S. Dowie, D.A. Whan, C. Kemball, J. Chem. Soc.-Faraday Trans. 68 (1972) 2150–2162.
[43] C. Kemball, Catal. Rev. 5 (1971) 23–53.
[44] C. Kemball, R. Brown, J. Chem. Soc.-Chem. Commun. (1987) 771–773.
[45] R.D. Cortright, R.M. Watwe, B.E. Spiewak, J.A. Dumesic, Catal. Today 53 (1999) 395–406.
[46] R.M. Watwe, R.D. Cortright, J.K. Norskov, J.A. Dumesic, J. Phys. Chem. B 104 (2000) 2299–2310.
[47] Z.-J. Zhao, L.V. Moskaleva, N. Rosch, J. Catal. 285 (2012) 124–133.
[48] R.D. Cortright, R.M. Watwe, J.A. Dumesic, J. Mol. Catal. A: Chem. 163 (2000) 91–103.
[49] D.W. Flaherty, E. Iglesia, J. Am. Chem. Soc. 135 (2013) 18586–18599.
[50] D.W. Flaherty, D. Hibbitts, E.I. Gürbüz, E. Iglesia, in preparation.
[51] G.B. McVicker, R.T.K. Baker, R.L. Garten, E.L. Kugler, J. Catal. 65 (1980) 207–220.
[52] M. Choi, Z.J. Wu, E. Iglesia, J. Am. Chem. Soc. 132 (2010) 9129–9137.
[53] M. Boudart, G. Djega-Mariadassou, The Kinetics of Heterogeneous Catalytic Reactions, Princeton University Press, Princeton, New Jersey, 1984.
[54] M. Schneider, D.G. Duff, T. Mallat, M. Wildberger, A. Baiker, J. Catal. 147 (1994) 500.
[55] G. Kresse, J. Furthmuller, Comput. Mater. Sci. 6 (1996) 15–50.
[56] G. Kresse, J. Furthmuller, Phys. Rev. B: Condens. Matter 54 (1996) 11169–11186.
[57] G. Kresse, J. Hafner, Phys. Rev. B: Condens. Matter 47 (1993) 558–561.
[58] G. Kresse, J. Hafner, Phys. Rev. B: Condens. Matter 49 (1994) 14251–14269.
[59] P.E. Blochl, Phys. Rev. B: Condens. Matter 50 (1994) 17953–17979.
[60] G. Kresse, D. Joubert, Phys. Rev. B: Condens. Matter 59 (1999) 1758–1775.
[61] B. Hammer, L. Hansen, J.K. Norskov, Phys. Rev. B: Condens. Matter 59 (1999) 7413–7421.
[62] J. Perdew, K. Burke, M. Ernzerhof, Phys. Rev. Lett. 77 (1996) 3865–3868.
[63] Y. Zhang, W. Yang, Phys. Rev. Lett. 80 (1998) 890.
[64] H.J. Monkhorst, J.D. Pack, Phys. Rev. B: Condens. Matter 13 (1976) 5188–5192.
[65] G. Henkelman, H.A. Jonsson, J. Chem. Phys. 113 (2000) 9978–9985.
[66] H.A. Jonsson, G. Mills, K.W. Jacobsen, Nudged Elastic Band Method for Finding Minimum Energy Paths of Transitions, World Scientific, 1998.
[67] G. Henkelman, H.A. Jonsson, J. Chem. Phys. 111 (1999) 7010–7022.
[68] J.H. Sinfelt, D.J.C. Yates, J. Catal. 8 (1967) 82–90.
[69] G.C. Bond, R.H. Cunningham, J. Catal. 166 (1997) 172–185.
[70] G.C. Bond, J.C. Slaa, J. Mol. Catal. A: Chem. 106 (1996) 135–149.
[71] A. Uzun, D.W. Flaherty, S.L. Soled, E. Iglesia, in preparation.
[72] D.W. Flaherty, E. Iglesia, Unpublished Work.
[73] J. Kua, F. Faglioni, W.A. Goddard, J. Am. Chem. Soc. 122 (2000) 2309–2321.
[74] S. Kawi, J.-R. Chang, B.C. Gates, J. Phys. Chem. 98 (1994) 12978–12988.
[75] I.M. Ciobica, A.M. Kleyn, R.A. van Santen, J. Phys. Chem. B 107 (2003) 164–172.
[76] C. Mager-Maury, G. Bonnard, C. Chizallet, P. Sautet, P. Raybaud, ChemCatChem 3 (2011) 200–207.
[77] B.J. Kip, F.B.M. Duivenvoorden, D.C. Koningsberger, R. Prins, J. Catal. 105 (1987) 26–38.
[78] R. van Hardeveld, F. Hartog, Surf. Sci. 15 (1969) 189–230.
[79] E.V. Anslyn, D.A. Dougherty, Modern Physical Organic Chemistry, University Science Books, Sausalito, CA, 2006.